Front. Earth Sci. 2023, 17(4): 1012–1025
https://doi.org/10.1007/s11707-023-1094-6

RESEARCH ARTICLE

Holocene temperature variation recorded by branched glycerol dialkyl glycerol tetraethers in a loess-paleosol sequence from the north-eastern Tibetan Plateau

Tianxiao WANG[1], Duo WU (✉)[1], Tao WANG[1], Lin CHEN[1], Shilong GUO[1], Youmo LI[1], Chenbin ZHANG[2]

1 Key Laboratory of Western China's Environmental Systems (Ministry of Education), College of Earth and Environmental Sciences, Lanzhou University, Lanzhou 730000, China

2 Alpine Paleoecology and Human Adaptation Group (ALPHA), Institute of Tibetan Plateau Research, Chinese Academy of Sciences, Beijing 100101, China

Abstract Reconstructing Holocene temperature evolution is important for understanding present temperature variations and for predicting future climate change, in the context of global warming. The evolution of Holocene global temperature remains disputed, due to differences between proxy reconstructions and model simulations, a discrepancy known as the 'Holocene temperature conundrum'. More reliable and quantitative terrestrial temperature records are needed to resolve the spatial heterogeneity of existing records. In this study, based on the analysis of branched glycerol dialkyl glycerol tetraethers (brGDGTs) from a loess-paleosol sequence from the Ganjia Basin in the north-eastern Tibetan Plateau (NETP), we quantitatively reconstructed the mean annual air temperature (MAAT) over the past 12 ka. The MAAT reconstruction shows that the temperature remained low during the early Holocene (12–8 ka), followed by a rapid warming at around 8 ka. From 8 to 4 ka, the MAAT record reached its highest level, followed by a cooling trend from the late Holocene (4–0 ka). The variability of the reconstructed MAAT is consistent with trends of annual temperature records from the Tibetan Plateau (TP) during the Holocene. We attribute the relatively low temperatures during the early Holocene to the existence of ice sheets at high-latitude regions in the Northern Hemisphere and the weaker annual mean insolation at 35°N. During the mid to late Holocene, the long-term cooling trend in the annual temperature record was primarily driven by declining summer insolation. This study provides key geological evidence for clarifying Holocene temperature change in the TP.

Received May 12, 2023; accepted August 16, 2023

E-mail: dwu@lzu.edu.cn

Keywords Holocene, Ganjia Basin, loess, temperature variation, BrGDGTs

1 Introduction

Since the Industrial Revolution, almost all regions of the globe have experienced warming, accompanied by climatic and environmental problems, including melting glaciers, rising sea levels and more frequent extreme climate events (IPCC, 2023). The temperature evolution of the current interglacial, the Holocene, and its mechanisms, provide a reference for predicting future climate change, which is a focus of climate change research. Marcott et al. (2013) stacked global annual temperature variations during the Holocene, illustrating a relatively high temperature from 10 to 5 ka and a cooling trend from 5 to 0.5 ka. Proxy reconstructions have been disputed by the results of model simulations. For example, Liu et al. (2014) simulated a long-term warming trend of global Holocene annual temperature, based on three coupled ocean-atmosphere models (CCSM3, FAMOUS, and LOVECLIM). The discrepancy between proxy reconstructions and model simulations is referred to as the 'Holocene temperature conundrum' which limits our understanding of the processes and mechanisms driving past temperature changes (Liu et al., 2014).

Some research suggests that climate models cannot accurately simulate Holocene temperature evolution due to their lack of feedback processes, including regional vegetation change, sea ice, and atmospheric dust (Liu et al., 2018; Hou et al., 2019; Park et al., 2019; Thompson et al., 2022). Studies of proxy records and their limitations focus on seasonal biases and spatial distribution. For example, new winter temperature

records from the Northern Hemisphere (NH) are enabling understanding of the pattern and mechanism of Holocene seasonal temperature variations (Meyer et al., 2015; Baker et al., 2017; Rao et al., 2020). Cartapanis et al. (2022) showed that the spatio-temporal structure of Holocene temperature modes is complex, with a discrepancy between terrestrial and marine proxy records from different latitudes. Therefore, it is necessary to select proxy records with a uniform spatial distribution to create a representative global temperature reconstruction. A number of recent studies have contributed to the global and regional databases of Holocene paleotemperature time series (Marsicek et al., 2018; Kaufman et al., 2020; Zhang et al., 2022b). The pollen-based terrestrial stack for North America and Europe shows an annual warming trend from the early to middle Holocene (10 to 5 ka), followed by a slightly declining variation until around 2 ka (Marsicek et al., 2018). A multi-proxy database of paleotemperature time series (Temperature 12k) has been established to enable a more robust reconstruction of Holocene temperature variability (Kaufman et al., 2020).

To correct the potential biases in the seasonality of records, Bova et al. (2021) present a seasonal to mean annual transformation (SAT) method, assuming that global seasonal temperature is directly responsive to seasonal insolation during the last inter-glacial period (128 to 115 ka). Although the assumption is disputed (Zhang and Chen, 2021; Laepple et al., 2022), the results showed that global sea surface temperature has slightly but steadily warmed, driven by rising atmospheric greenhouse gas (GHG) concentrations and shrinking ice sheets (Bova et al., 2021). By using a paleoclimate data assimilation, Osman et al. (2021) found a general warming trend in global surface temperatures over the past 24 kyr and attributed the Holocene temperature conundrum to the uneven spatial distribution of proxy records. Pollen-based reconstructions over the NH landmass showed that annual, summer and winter temperatures warmed from 11 to 7 ka and cooled thereafter. Summer solar radiation in the Northern Hemisphere may cross-seasonally affect winter and annual temperatures via feedback processes involving vegetation and sea ice (Zhang et al., 2022c). Annual and seasonal temperatures from mollusk-based records showed a cooling trend, indicating that seasonal biases in proxies may not be the primary cause of data-model inconsistencies (Dong et al., 2022). Several unresolved issues concerning temperature proxies remain, in particular their uneven spatial distribution, and seasonal biases (Kaufman and Broadman, 2023). Quantitative paleotemperature reconstructions, based on reliable indicators and from previously under-represented regions, are needed to describe global and regional Holocene temperature changes in more detail.

As the largest and highest plateau in the world, the Tibetan Plateau (TP) is rich in glaciers, frozen soils, lakes and rivers, and provides water for more than a third of the world's population (Qiu, 2008; Immerzeel et al., 2010; Immerzeel et al., 2020). Modern observations show that the TP is experiencing rapid retreat of glaciers and massive expansion of lakes (Yao et al., 2019; Immerzeel et al., 2020), accompanied by dramatic temperature fluctuations and glacier instability (Bolch et al., 2012; Jacob et al., 2012; Neckel et al., 2014). There are many palaeotemperature reconstructions in the TP and surrounding areas based on geological archives, such as loess deposits (Sun et al., 2019; Wang et al., 2021), ice cores (Pang et al., 2020), lacustrine sediments (Wu et al., 2018; Han et al., 2020; Wang et al., 2021; Zhang et al., 2022b) and peat sediments (Yan et al., 2021). Multi-proxy reconstructions of Holocene temperature patterns in the TP and its surrounding areas are disputed. For example, the summer temperature reconstructions—based on alkenone form Qinghai Lake, fossil chironomids from Tiancai Lake, and pollen form Xingyun Lake, respectively—display overall cooling trends (Hou et al., 2016; Zhang et al., 2017; Wu et al., 2018). For high altitude lakes, ice-free-season temperatures, inferred from branched glycerol dialkyl glycerol tetraethers (brGDGTs), show a long-term warming trend in Tingming Lake and Cuoqia Lake (Sun et al., 2021; Zhang et al., 2022b). In contrast, the δ^{18}O-inferred winter temperature informed from the Chongce ice core shows a generally warming trend (Pang et al., 2020). The Holocene annual temperature variation over the TP is relatively complex, and can be roughly divided into three modes. First, brGDGTs-inferred annual temperature records mainly display a generally warming trend at Tiancai Lake, Tengchongqinghai Lake, and Hongyuan peatland, over the eastern TP (Yan et al., 2021; Zhao et al., 2021b; Feng et al., 2022). Second, the reconstructed annual mean temperature shows a cooling-warming pattern at both SHD09 section and Aweng Co in the north-eastern and western TP (Li et al., 2017; Wang et al., 2021). Third, the reconstructions based on pollen record stacks and brGDGTs proxies show that annual mean temperature experiences a generally cooling trend (Sun et al., 2019; Chen et al., 2020; Han et al., 2020). Therefore, additional quantitative proxy-based-temperature reconstructions are required to understand Holocene temperature change over the TP more comprehensively.

The brGDGTs are produced by unknown bacteria and well preserved in natural archives including loess and peats (Schouten et al., 2013). The compound is widely regarded as a reliable proxy of palaeotemperature, due to its sensitivity to environmental changes (Peterse et al., 2011; Feng et al., 2019; Wang et al., 2021). BrGDGTs compounds have been developed into a series of independent alternative proxies and temperature transfer functions (Weijers et al., 2007; Peterse et al., 2012; De Jonge et al., 2014; Yang et al., 2014; Naafs et al., 2017; Dearing Crampton-Flood et al., 2020). Weijers et al.

(2007) first defined the methylation index of branched tetraethers (MBT) and cyclisation ratio of branched tetraethers (CBT, Eq. (1)) proxies, and established temperature and pH calibration equations. To eliminate the uncertainty of brGDGTs proxies in reconstructing terrestrial palaeotemperature, methods including extending the global data set, performing local brGDGTs calibrations, establishing new proxies and statistical methods have been proposed (Table 1 and Table 2). For example, Peterse et al. (2012) suggested a new proxy marked as MBT' (Eq. (2)) and a new calibration equation (Eq. (7)) with an updated data set. The 6-methyl brGDGTs compounds are separated by De Jonge et al. (2013). De Jonge et al. (2014) defined the MBT'_{5ME} index (Eq. (3)) with exclusion of the 6-methyl brGDGTs from the MBT' and global MBT'_{5ME} calibration (Eq. (8)). A new proxy defined as $MBT_{5/6}$ (Eq. (4)) and regional calibrations ((Eq. (9) and Eq. (10)) with brGDGTs data set in the TP were proposed (Ding et al., 2015). Dang et al. (2016) proposed a new proxy, the IR_{6ME} (relative abundance of 6-methyl brGDGTs) index, to assess the applicability of brGDGTs-based paleotemperature reconstructions and indicated that the MBT' index can reconstruct temperature reliably only if the IR_{6ME} value is less than 0.5. Subsequently, the IR_{6ME} index can evaluate the credibility of temperature reconstructions based on the MBT'_{5ME} proxy (Naafs et al., 2017; Crampton-Flood et al., 2020). The MBT'_{5ME} proxy has been shown to be unable to reconstruct paleotemperature in global soil or peat data sets when the value of the community index (CI, Eq. (6)) exceeds 0.64 (De Jonge et al., 2019). Recently, Véquaud et al. (2022) and Zhao et al. (2022) significantly improved the accuracy of the previous global terrestrial brGDGTs temperature calibration using nonlinear models. Overall, despite the large number of global and regional brGDGTs temperature calibrations, the reliably assessing temperature indicators and selecting the best available temperature calibration is key to paleotemperature reconstructions of loess-paleosol sequences.

Here we present a new brGDGTs record from a loess-paleosol sequence from the Ganjia Basin and reconstruct Holocene paleotemperature variability in the north-eastern TP. We demonstrate the reliability of the reconstructed temperature and compare our reconstruction with previously reported records over the TP and its surrounding area to elucidate the temperature patterns and possible forcing mechanisms.

2 Study site

The Ganjia Basin is located in the north-eastern margin of the TP, in the northern part of Xiahe County, Gannan Tibetan Autonomous Prefecture, Gansu Province (Fig. 1). The east–west and north–south lengths of the Ganjia Basin are about 23 and 18 km, respectively, with an altitude of 2821 to 3200 m above sea level (a.s.l.) (Wu et al., 2021; Zhang et al., 2022a). The regional climate is strongly impacted by the East Asian summer monsoon (EASM) and the mid-latitude Westerlies, and characterized by highland continental climates (An et al., 2012; Chen et al., 2020; Li et al., 2020). Observations from meteorological stations at Xiahe County show that the average annual precipitation and temperature were 448 mm and 3.4°C from 1981−2010. The precipitation between May and September contributes to more than 80% of the annual precipitation, controlled by the south-easterly EASM. In winter, the regional climate is cold and

Table 1 Calculation of the brGDGTs temperature indices

Proxy	Calculation	Referencesx	Equation No.
CBT	$-\log[(Ib + IIb + IIb')/(Ia + IIa + IIa')]$	Weijers et al. (2007)	(1)
MBT'	$(Ia + Ib + Ic)/(Ia + Ib + Ic + IIa + IIa' + IIb + IIb' + IIc + IIc' + IIIa + IIIa')$	Peterse et al. (2012)	(2)
MBT'_{5ME}	$(Ia + Ib + Ic)/(Ia + Ib + Ic + IIa + IIb + IIc + IIIa)$	De Jonge et al. (2014)	(3)
$MBT_{5/6}$	$(Ia + Ib + Ic + IIa')/(Ia + Ib + Ic + IIa + IIb + IIc + IIIa + IIIa')$	Ding et al. (2015)	(4)
IR_{6ME}	$(IIa' + IIb' + IIc' + IIIa' + IIIb' + IIIc')/(IIa' + IIb + IIb' + IIc + IIc' + IIIa + IIIa' + IIIb + IIIb' + IIIc + IIIc')$	Dang et al. (2016)	(5)
CI	$(Ia)/(Ia + IIa + IIIa)$	De Jonge et al. (2019)	(6)

Table 2 Formulae for the global and regional calculations of brGDGTs temperature indices

Material	Calculation	References	Equation No.
Global soils data set	$MAAT = 0.81 - 5.67 \times CBT + 31.0 \times MBT'$ ($n = 176$, $R^2 = 0.59$, RMSE = 5.0°C)	Peterse et al. (2012)	(7)
Global soils data set	$MAAT = 31.45 \times MBT'_{5ME} - 8.57$ ($n = 222$, $R^2 = 0.66$, RMSE = 4.8°C)	De Jonge et al. (2014)	(8)
TP soils data set	$MAAT = 28.36 \times MBT'_{5ME} - 10.82$ ($n = 27$, $R^2 = 0.65$, RMSE = 1.8°C)	Ding et al. (2015)	(9)
TP soils data set	$MAAT = 39.51 \times MBT_{5/6} - 20.14$ ($n = 27$, $R^2 = 0.82$, RMSE = 1.3°C)	Ding et al. (2015)	(10)
China soils data set	$MAAT = 42.6 \times MBT'_{5ME} - 21.0$ ($n = 149$, $R^2 = 0.75$, RMSE = 4.3°C)	Wang et al. (2020)	(11)

dry, under the influence of the westerly winds and the East Asian winter monsoon (EAWM). The regional vegetation type is alpine grassland, dominated by sedge and grasses, with subalpine meadow soil (Shang and Jin, 2012). The study area is adjacent to the western part of the Chinese Loess Plateau (CLP), and widely distributed in the foothills of the basin and on top of the river terraces.

3 Materials and methods

3.1 Sampling and chronology

The BSY19A section of the study area (BSY19A) (35°26′24.80″N, 102°34′2.14″E, 3191 m a.s.l.) is located on the southern slopes of the Dalija Mountains, northern Ganjia Basin. Field surveying revealed that the section has a typical aolian deposit profile, with a stable depositional environment and clear stratigraphic boundaries between the loess and paleosol layers (Fig. 2(a)). The BSY19A section is 140-cm thick. The uppermost 10 cm of the section presents abundant plant roots, with no evidence of human farming activities. According to our fieldwork and proxies (Fig. 2) including magnetic susceptibility, mean grain size, and organic carbon isotopes, we divided the BSY19A profile into three main layers: 1) topsoil layer: 0−10 cm, dark brown and indurated, with plant roots throughout; 2) paleosol layer: 10−75 cm, dark brown clayey silt with crumb structure and bio-pores; 3) loess layer: 75−140 cm, yellowish to light brown silt with a compact structure.

A total of 140 sediment samples were collected at 1 cm intervals from the BSY19A section. Twelve bulk organic samples, with a relatively equal interval were selected, and their ages were measured using the accelerator mass spectrometry (AMS) ^{14}C dating method. AMS was carried out by Beta Analytic, USA. The age-depth model was built using the R software package 'Bacon model'. The chronology of the loess-paleosol deposits were also established, with their reliability confirmed by comparing it with the optically stimulated luminescence (OSL) dating of an adjacent section (Wu et al., 2021).

3.2 GDGTs analysis

We selected 16 sediment samples with equal age intervals and picked out plant roots and gravels from the samples. The 50 g air-dried samples were ground into powders and were screened using a 60-mesh sieve. We used an Accelerated Solvent Extractor (ASE 350, Thermo Fisher) to extract the total lipid content using dichloromethane (DCM): methanol (MeOH) (9:1, v/v). The total extracts were condensed by a rotary evaporator and separated over a silica gel using hexane, dichloromethane, and methanol eluents to obtain apolar and polar fractions (containing GDGTs). We dried the polar fractions under continuous nitrogen (N_2) flow, followed by redissolving and filtering them through a 0.22 μm PTFE filter (Wang et al., 2022).

The brGDGTs were analyzed using an Agilent 1290 series ultraperformance liquid chromatography-atmospheric pressure chemical ionization–6465B triple

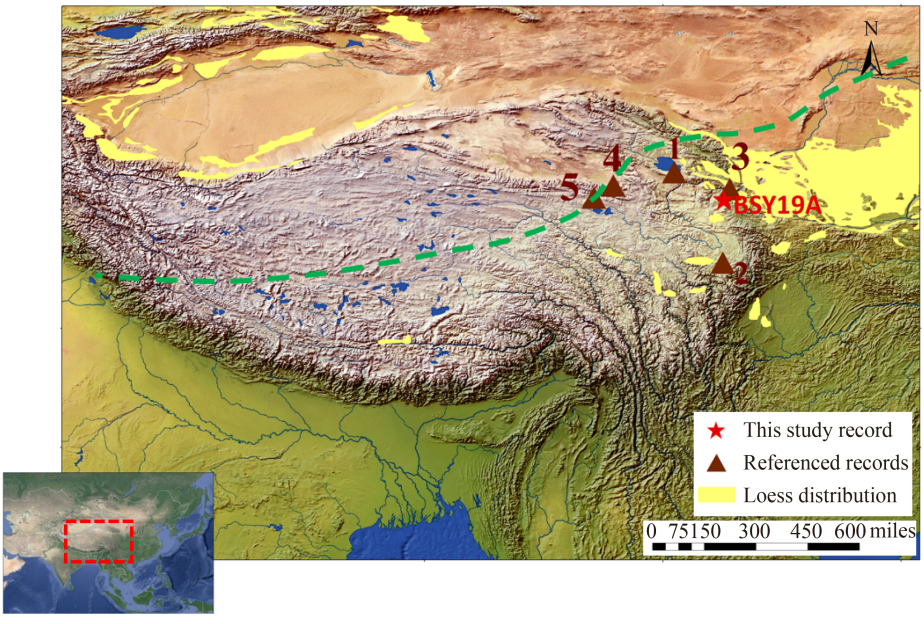

Fig. 1 Locations of the BSY19A loess section and the temperature records referenced in the paper. Numbered brown triangles show locations of 1) YWY14 section (Wang et al., 2021); 2) Hongyuan Peatland (Yan et al., 2021); 3) Shanglajia section (Zhao et al., 2018); 4) Xiangride section (Sun et al., 2019); 5) Alake Lake (Han et al., 2020). The green dashed line represents the northern boundary of the modern East Asian summer monsoon (Chen et al., 2008). The yellow shaded areas are loess distributions.

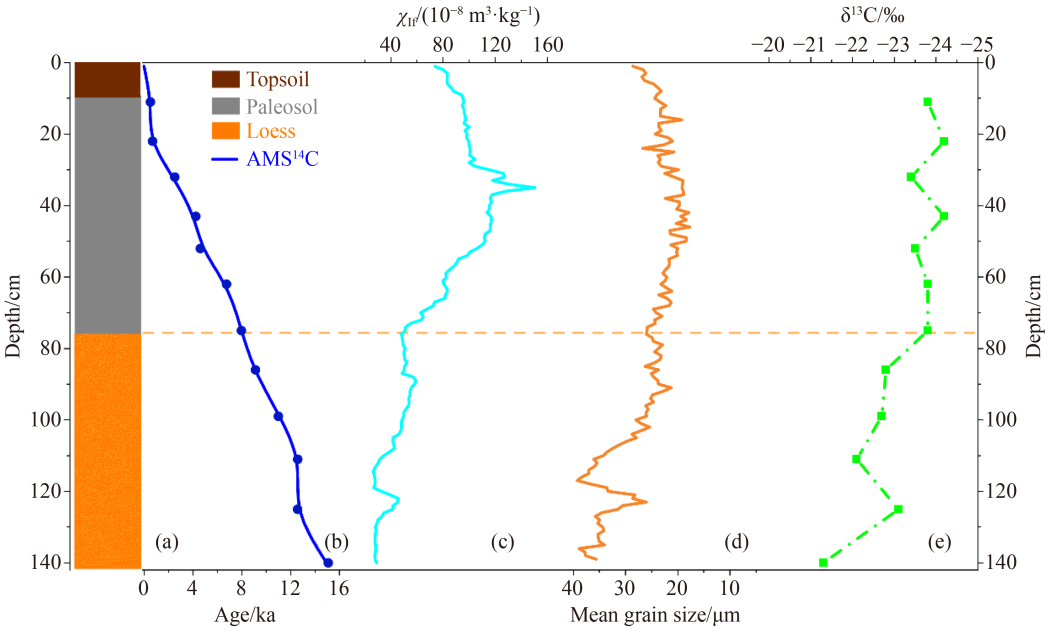

Fig. 2 Lithology (a), age-depth model (b), and proxy records of magnetic susceptibility (c), mean grain size (d), and δ^{13}C (e) for loess section BSY19A (Wu et al., 2021).

quadrupole mass spectrometry (UPLC-APCI-MS) system. Separation was achieved using three Hypersil GOLD Silica columns in sequence (each 100 mm × 2.1 mm, 1.9 μm, Thermo Fisher Scientific) and maintained at 40°C, with a flow rate of 0.2 mL/min. The injection volume was 20 μL.

Following similar methods, the mobile phase A is *n*-hexane, and B is EtOA. The brGDGTs were eluted isocritically with 84% A and 16% B for first five minutes, followed by the elution gradient change to 84% A: 16% B from 5 to 65 min (Wang et al., 2022). The following elution gradient was then used: 100% B, from 65 to 80 min, then 84% A and 16% B to equilibrate the pressure. We used the selective ion monitoring (SIM) mode to track brGDGTs at m/z ratios of 1050, 1048, 1046, 1036, 1034, 1032, 1022, 1020, and 1018. The brGDGTs compounds were identified as IIIa (IIIa′), IIIb (IIIb′), IIIc (IIIc′), IIa (IIa′), IIb (IIb′), IIc (IIc′), Ia, Ib, and Ic, followed by quantification from the integrated peak area of the $[M + H]^+$ ions. The concentration of the internal C_{46}GDGT standard is 0.001157 ng/mL. The experiments described above were conducted at the Key Laboratory of Western China's Environmental Systems (Ministry of Education), Lanzhou University.

4 Results

4.1 Distribution of brGDGTs in the BSY19A section

All the expected components of brGDGTs were detected in the samples of BSY19A profile. Their total concentration varies between 0.04 and 20.6 ng/g, with a mean value of 6.79 ng/g. BrGDGT-IIIa′ and IIb′ were the most abundant compounds (38%) in BSY19A section, followed by brGDGT-IIa′, IIIa and Ia. The relative abundances of cyclic brGDGTs components (i.e., brGDGT-IIb, IIc) are slightly higher than that of major acyclic brGDGTs (i.e., brGDGT-IIa).

The IR_{6ME} index values are higher than 0.6 in all samples, revealing that the relative abundance of 5-methyl brGDGTs is lower than 6-methyl brGDGTs. The CI index values varied from 0.2 to 0.4, with a mean value of 0.28 (Table 3). There are significant differences in the distribution characteristics of brGDGTs compounds between the loess and paleosol samples, including brGDGT-IIIb′, IIIc′, IIc′, and IIa′. Compared to the paleosol samples, we observe lower brGDGT-IIa′ and higher brGDGT-IIIc′, IIc′, and IIIb′ in loess samples (Fig. 3).

Figure 4 shows that the relative abundance of pentamethylation is highest (52%), followed by hexamethylation (35%), while tetramethylation is the least abundant compound (13%). The distribution characteristics of pentamethylation and hexamethylation in the BSY19A profile differed significantly from those of global soils, Chinese soils, and north-eastern TP soils, which demonstrate higher proportion of pentamethylation and lower proportion of hexamethylation.

4.2 Reconstructed Holocene MAAT variations from the BSY19A section

The value of the CBT index shows long-term stability, with an absolute mean value of −0.03 in the BSY19A profile. Meanwhile, the absolute value of the $MBT_{5/6}$

Table 3 The brGDGTs concentrations and proxy records of IR_{6ME}, CI, MBT', $MBT_{5/6}$, and MBT'_{5ME} for the BSY19A profile

Age/ka	IR_{6ME}	CI	Concentration/ ($ng \cdot g^{-1}$)	MBT'_{5ME}	MBT'	$MBT_{5/6}$	CBT
0.12	0.81	0.30	41.33	0.38	0.11	0.56	0.32
0.91	0.77	0.26	29.77	0.37	0.12	0.63	−0.01
1.80	0.77	0.31	40.01	0.41	0.14	0.67	−0.01
2.85	0.73	0.32	18.90	0.41	0.16	0.65	−0.12
3.75	0.73	0.30	1.91	0.40	0.16	0.56	−0.07
4.67	0.73	0.38	8.11	0.45	0.19	0.63	−0.04
6.57	0.74	0.40	9.43	0.47	0.19	0.66	−0.02
7.44	0.72	0.35	9.53	0.44	0.18	0.60	−0.01
8.36	0.65	0.20	0.08	0.28	0.18	0.38	−0.06
9.39	0.67	0.22	11.73	0.28	0.12	0.47	−0.12
10.30	0.69	0.21	13.12	0.28	0.11	0.50	−0.15
11.23	0.69	0.19	10.87	0.26	0.11	0.50	−0.08
12.15	0.73	0.22	13.17	0.29	0.11	0.48	−0.09
13.02	0.77	0.22	4.06	0.35	0.12	0.44	−0.22
14.04	0.78	0.22	2.45	0.34	0.11	0.42	−0.28
14.94	0.77	0.20	2.97	0.31	0.10	0.38	−0.26

index is characterized by a pattern of lower values during the early Holocene, followed by higher values during the middle to late Holocene, with a mean value of 0.56. Notably, the MBT'_{5ME} and MBT′ indices vary consistently with each other. The absolute values of the indices remain low during the early Holocene and reach a maximum at 6.5 ka, followed by a gradual declining trend. The ranges of the MBT'_{5ME} and MBT′ indices variations are 0.26−0.47 and 0.11−0.19, respectively (Fig. 5).

Previously published temperature transfer functions have been based on independent brGDGTs proxies (i.e., MBT′, MBT'_{5ME}, and $MBT_{5/6}$) and the modern soil data sets, including global soils, Chinese soils and TP soils (Peterse et al., 2012; De Jonges et al., 2014; Ding et al., 2015; Wang et al., 2020). The brGDGTs-based temperature variations at section BSY19A during the Holocene were reconstructed using the temperature calibrations described in Section 1 (Table 2). The temperature reconstructions from these transfer functions were strongly correlated with each other, and revealed relatively cold temperatures between 12 ka and 8 ka, followed by a rapid warming at approximately 8 ka, and a general cooling trend from 6 ka to present (Fig. 6). However, a large difference in the amplitude of variation of the above reconstructions occurred, which is most apparent in the reconstruction based on Eq. (9) (11.46°C).

5 Discussion

5.1 The assessment of reconstructed MAAT records in the BSY19A section

The MBT and its derived indicators have been proven to indicate MAAT, and this has been applied to paleotemperature reconstructions for loess and paleosol sequences (Weijers et al., 2007; Peterse et al., 2012; De Jonge et al., 2014). With continued expansion of the soil data set and the emergence of new indicators (i.e., MBT', $MBT_{5/6}$ and MBT'_{5ME}), two new indices (IR_{6ME} and CI) assess the confidence of the brGDGTs proxies for reconstructing temperatures (Dang et al., 2016; De Jonge et al., 2019). The accuracy of the brGDGTs index for temperature reconstruction must therefore be tested by the IR_{6ME} and CI indices. Given the potential existence of a summer bias in brGDGTs proxies, analysis of the TP soil data set is needed (Deng et al., 2016; Cao et al., 2018; Crampton-Flood et al., 2020).

In this study, we collected the current published data set of surface soils on the TP (n = 127; Naafs et al., 2017; Dearing Crampton-Flood et al., 2020; Wang et al., 2020; Wang and Liu, 2021) and investigated the correlation between brGDGTs indices and local MAAT, and warmest month air temperature (WMT). Figure 7 shows a significant positive correlation of both MBT' and MBT'_{5ME} with local MAAT (r = 0.56 and 0.61), respectively. The correlation between $MBT_{5/6}$ and local MAAT is lower (r = 0.39). Compared with the MAAT, the correlation between MBT'_{5ME} index and WMT was slightly higher in TP soils (r = 0.61 and 067, respectively), demonstrating that the MBT'_{5ME} index can

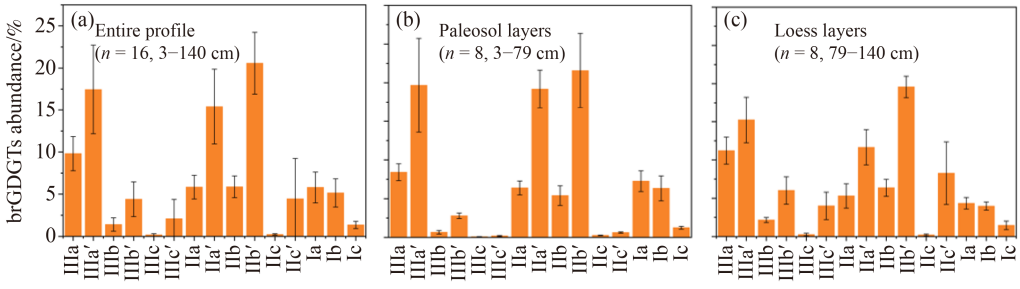

Fig. 3 Comparison of the fractional abundances of brGDGTs in the entire BSY19A profile (a), paleosol layers (b), and loess layers (c).

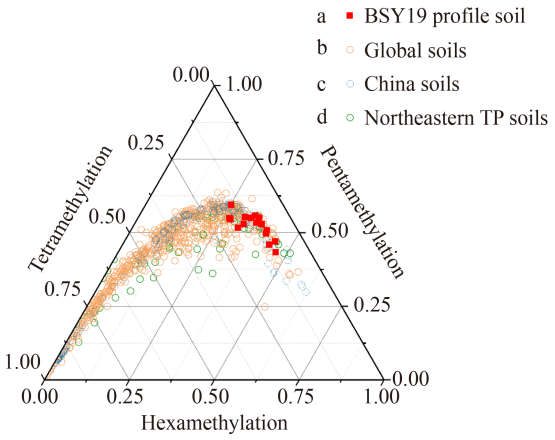

Fig. 4 Comparison of the fractional abundances of brGDGTs for the BSY19A profile (a) with previously published data, including global soils (b, Crampton-Flood et al., 2020); China soils (c, Wang et al., 2020); NETP soils (d, Chen et al., 2019; Wang and Liu, 2021; Wang et al., 2022).

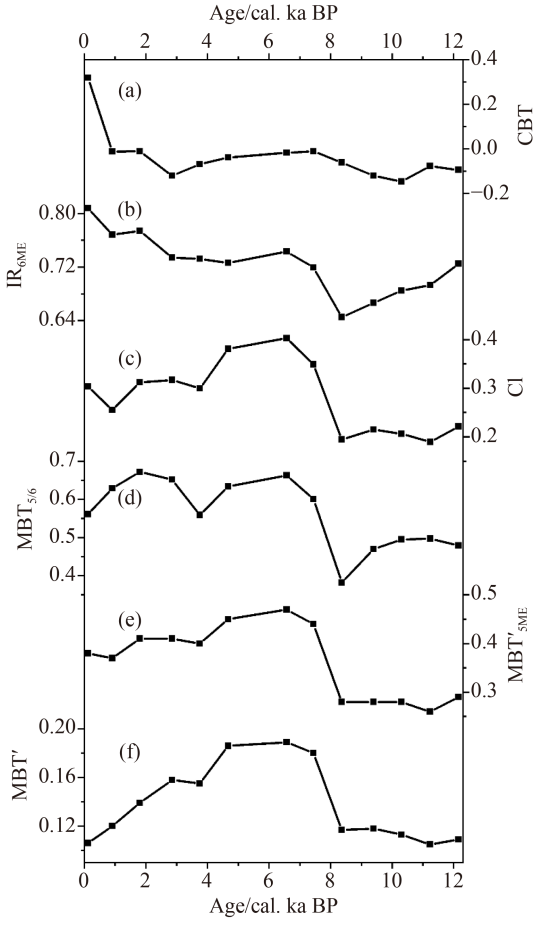

Fig. 5 Variation of brGDGTs-derived proxy records in the BSY19A profile, including (a) CBT, (b) IR_{6ME}, (c) CI, (d) $MBT_{5/6}$, (e) MBT'_{5ME}, and (f) MBT'.

indicate MAAT, despite the possible warm season bias in the MBT'_{5ME} index. We extracted soil samples with $IR_{6ME} > 0.5$ and CI < 6.4 from the original TP soil data

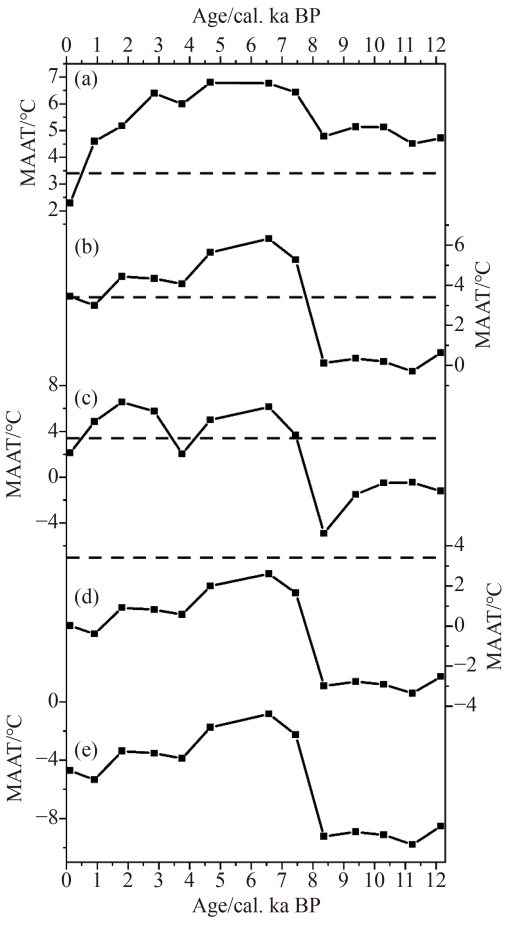

Fig. 6 Comparisons of MAAT reconstructed from different transfer functions based on the global data set (a; Peterse et al., 2012); global data set (b; De Jonges et al., 2014); TP data set (c, d; Ding et al., 2015); Chinese data set (e; Wang et al., 2020). The dashed lines represent the local modern instrumental MAAT.

set (n = 77) and found that the resulting correlations between MBT'_{5ME} and MAAT or MWT are slightly different (r changes from 0.61 to 0.63 and from 0.67 to 0.65, respectively). We therefore conclude that the IR_{6ME} and CI indicators have only a minor effect on the correlation between MBT'_{5ME} and MAAT or MWT.

We reconstructed the modern MAAT in BSY19A section based on different transfer functions and found that the modern MAAT based on Eq. (8) (3.45°C; Table 4) agrees well with the instrumental MAAT (3.4°C), for the period from 1981 to 2010. The Holocene MAAT variation range (−0.28–6.32°C) reconstructed by the transfer equation from De Jonge et al. (2014) is more consistent with that of other records, for example the SHD09 and YWY14 profiles (Wang et al., 2021). Therefore, this global transfer equation can reliably reconstruct the modern and past temperature variations of the BSY19A profile (De Jonge et al., 2014).

The MAAT record presented here shows a low temperature (~ 0°C) during the early Holocene (12–8 ka) and a rapid warming at approximately 8 ka, followed by a

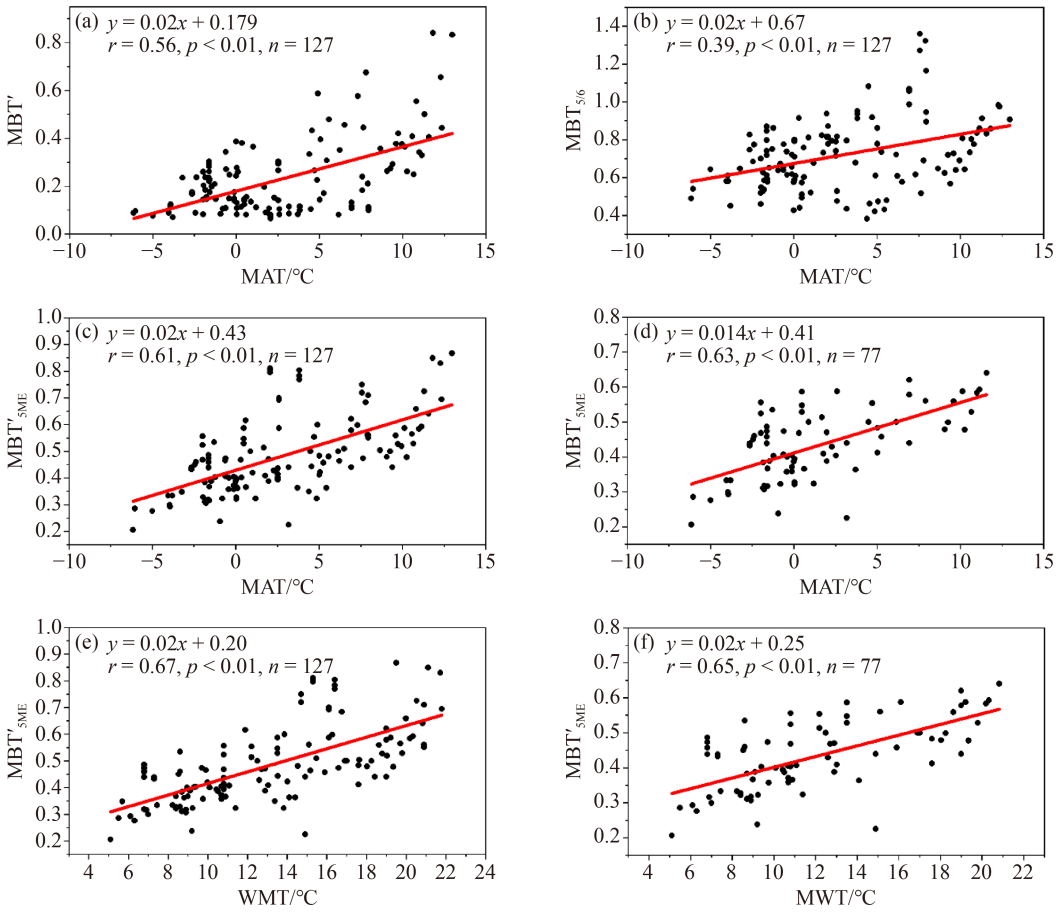

Fig. 7 Scatter plots of MAAT and MWT versus MBT' (a), $MBT_{5/6}$ (b), and MBT'_{5ME} (c, d, e, f) in TP soils (n = 127; Naafs et al., 2017; Crampton-Flood et al., 2020; Wang et al., 2020, 2021). The soil data sets in (d) and (f) are from soil samples with IR_{6ME} > 0.5 and CI < 0.64 (n = 77).

Table 4 Temperature reconstructions based on transfer functions for the BSY19A profile

Temperature/°C	MAAT [7]	MAAT [8]	MAAT [9]	MAAT [10]	MAAT [11]
Modern value	3.44	3.22	3.49	−0.18	−5.02
Maximum	6.80	6.32	6.55	2.61	−0.83
Minimum	2.29	−0.28	−4.91	−3.35	−9.78
Amplitude value	4.51	6.60	11.46	5.96	8.95

high temperature during the mid-Holocene (approximately 8−4 ka) and a long-term cooling from ~4 ka to present.

5.2 Paleotemperature variations on the TP and its surrounding regions during the Holocene

We reviewed previously published multi-proxy-based temperature records of the TP and its surrounding regions during the Holocene, to systematically analyze the spatial pattern of temperature variability. We identified three MAAT patterns in the TP, including a general cooling mode, a continuous warming mode, and a cooling-warming mode. We found that the three modes mentioned in Section 1 have no obvious spatial coherence. For example, the continuous warming mode occurred at Hongyuan peatland, Tiancai Lake, Lugu Lake, and Naleng Co in the south-eastern and eastern TP (Opitz et al., 2015; Yan et al., 2021; Zhao et al., 2021b; Feng et al., 2022). The cooling-warming mode was reported in the YWY and SHD09 loess profiles, Aweng Co, and Linggo Co in the north-eastern, central, and western TP (Li et al., 2017; He et al., 2020; Wang et al., 2021).

Previous studies have shown that multiple proxies, including from pollen, alkenones, and fossil chironomids, are seasonally biased and can be used to reconstruct summer temperature (Liu et al., 2014; Marsicek et al., 2018; Bova et al., 2021). Reconstructions demonstrate a dominant, long-term decreasing summer solar radiation

during the Holocene (Zhang et al., 2022b). For example, a long-term cooling pattern occurs in the fossil chironomid record from Tiancai Lake, the alkenones record from Qinghai Lake, and the pollen record from Xingyun Lake (Hou et al., 2016; Zhang et al., 2017; Wu et al., 2018). Most of the MAAT records of the TP were reconstructed from the brGDGTs proxies, in which the existence of a warm-season bias remains disputed (Deng et al., 2016; Cao et al. 2018; Crampton-Flood et al., 2020). Therefore, we assume that the MAAT mode across the TP may not be affected by the spatial distribution of temperature records with seasonal biases. Despite the three patterns mentioned above, the overall magnitude of temperature changes is similar with each other in the TP. For example, the brGDGTs-inferred MAAT record from the YWY14 section displays an early to mid-Holocene decline of approximately 6°C and a mid to late-Holocene increase of approximately 5°C (Wang et al., 2021; Fig. 8(d)). A pollen-inferred MAAT record from Ximen Co showed a rapid warming of 3.5°C from 12 to 10 ka, and a continued high level from 10 to 5 ka, followed by a cooling of 2°C (Herzschuh et al., 2014). The MAAT pattern from Hongyuan peatland recorded Holocene thermal maximum during 7–5 ka (Yan et al., 2021; Fig. 8(b)). However, compared to the temperature records from the NETP, the amplitude of the Hongyuan peatland record was more than 10°C higher, a finding which was attributed to environmental factors including local altitude, vegetation cover, and differences in geological vectors. In summary, the complex spatial variation in temperature variability across regions of the NETP implies that more temperature records are needed to clearly describe the MAAT variation in the TP. The pattern observed in the present MAAT record is in broad agreement with numerous terrestrial temperature records and stacks for the Northern Hemisphere, including the global mean surface temperature for the latitude band of 30°N–60°N (Lu et al., 2022; Fig. 8(a)), the pollen-based temperature stack for the Northern Hemisphere landmass (Zhang et al., 2022c), and the pollen-based MAAT stack for the TP (Chen et al., 2020; Fig. 8(g)). The mid-Holocene thermal maximum was widespread across the mid-latitudes of the Northern Hemisphere landmass (Cartapanis et al., 2022; Zhang et al., 2022a).

We found that the relatively low temperature during the early Holocene occurred across the entire TP, as identified in records including from Ximen Co, Hongyuan peatland, Ximenglongtan Lake, and Tiancai Lake (Herzschuh et al., 2014; Ning et al., 2019; Yan et al., 2021; Feng et al., 2022). This low temperature was also reported in the core regions impacted by the EASM, including Nanyi Lake, Shuizhuyang peat bog, and Huguangyan Lake (Wang et al., 2017; Zhao et al., 2021a; Li et al., 2022). Long-term cooling patterns during the mid to late Holocene were also detected in the MAAT records of the NETP and the western edge of the CLP,

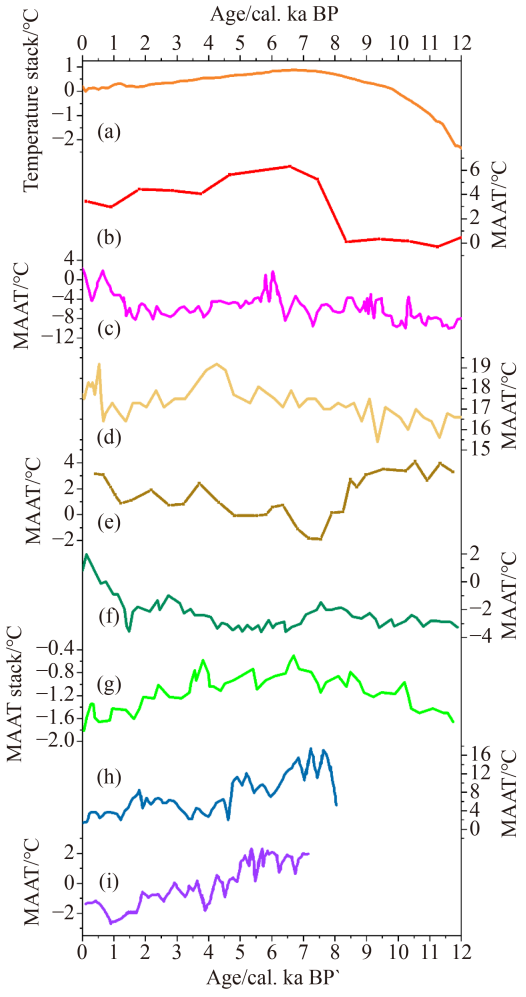

Fig. 8 Comparison between Holocene MAAT records from the north-eastern TP and other records in the adjacent regions. (a) Temperature stack for the latitude band of 30°N–60°N (Lu et al., 2022), (b) MBT'_{5ME}-based MAAT record for BSY19A section (this study), (c) brGDGTs-based MAAT record from Hongyuan Peatland (Yan et al., 2021), (d) brGDGTs-based MAAT record from Tengchongqinghai Lake (Zhao et al., 2022), (e) brGDGTs-based MAAT record from YWY loess profile (Wang et al., 2021), (f) brGDGTs-based MAAT record from Bangong Co (Wang et al., 2021), (g) pollen-based MAAT stack for the entire TP (Chen et al., 2020), (h) brGDGTs-based MAAT record from Alake Lake (Han et al., 2020), (i) brGDGTs-based MAAT record from Xiangride section (Sun et al., 2019).

including at sites in the Shanglajia section (Zhao et al., 2018), Alake Lake (Han et al., 2020; Fig. 8(h)), and Xiangride section (Sun et al., 2019; Fig. 8(i)). The gradual decrease of about 3°C at Ganjia Basin is similar to the MAAT record (~4°C) at the adjacent Shanglajia section (Zhao et al., 2018).

5.3 Possible mechanisms for the observed Holocene temperature evolution in the north-eastern TP

A series of Holocene climate forcings and feedbacks have been proposed, including the orbital-induced insolation,

ice volume of high latitudes, and atmospheric greenhouse gas concentrations, to provide a mechanism which explains Holocene temperature variability at the millennial scale (Wu et al., 2018; Wang et al., 2021; Duan et al., 2022; Feng et al., 2022; Li et al., 2022; Zhang et al., 2022b, 2022c). From the early Holocene, the low-temperature mode is widespread in the eastern TP and the EASM core regions. We infer that this mode may be closely related to climate-driven mechanisms at large spatial scales. The coupled global ocean–atmosphere–vegetation model results showed that the Northern Hemisphere continental ice sheets and their glacial meltwater provided a cooling effect on early Holocene climate, delaying the thermal maximum to the mid-Holocene over the mid to high latitudes of the Eurasian landmass (Renssen et al., 2009). The $^{231}Pa/^{230}Th$ record of a sediment core from the subtropical North Atlantic Ocean, a kinematic proxy for the Atlantic meridional overturning circulation (AMOC), maintained a relatively high value from 12 to 8 ka, indicating a weak AMOC (McManus et al., 2004; Fig. 9(b)). During the early Holocene, the remnant continental ice sheets at high latitudes in the Northern Hemisphere, specifically the Laurentide ice sheet (LIS), are therefore potentially important drivers of temperature variability.

During the early Holocene, the high-latitude continental ice sheets of the Northern Hemisphere, the LIS and Scandinavian ice sheets, would have cooled atmospheric temperatures in the high and mid-latitudes of the Northern Hemisphere in two ways. First, the ice sheets could induce a stable anticyclone by maintaining a strong albedo effect (Beghin et al., 2015). Secondly, the continued melting of the Northern Hemisphere ice sheet, in particular the LIS, could deliver fresh water to the North Atlantic Ocean (Dyke, 2004; Fig. 9(c)). Both processes would result in the expansion of sea ice in the North Atlantic and weakening of the AMOC (Sun et al., 2012). The temperature in the high latitudes of Eurasia in the early Holocene is at lower levels due to the weakening of latent heat transport from lower latitudes (Carlson et al., 2008; Alder and Hostetler, 2015; Mjell et al., 2015; Baker et al., 2017). This process results in a larger longitudinal temperature gradient from the mid to high latitudes (Lu et al., 2022; Fig. 9(d)) and stronger mid-latitude westerlies and EAWM during the early Holocene (An et al., 2012; Fig. 9(e); Li and Morrill, 2015; Fig. 9(f); Wu et al., 2021). The cold, northern branch of the mid-latitude westerlies and the East Asian winter winds can have a significant cooling effect on the climate of the NETP. The lowest annual insolation intensity in the Ganjia Basin is a potential cause of the relatively low temperatures during the early Holocene (Laskar et al., 2004; Fig. 9(g)). During the mid to late Holocene, a gradual temperature decline was recorded in our MAAT record and in summer temperature records from Qinghai Lake, Cuoqia Lake, Tiancai Lake, and

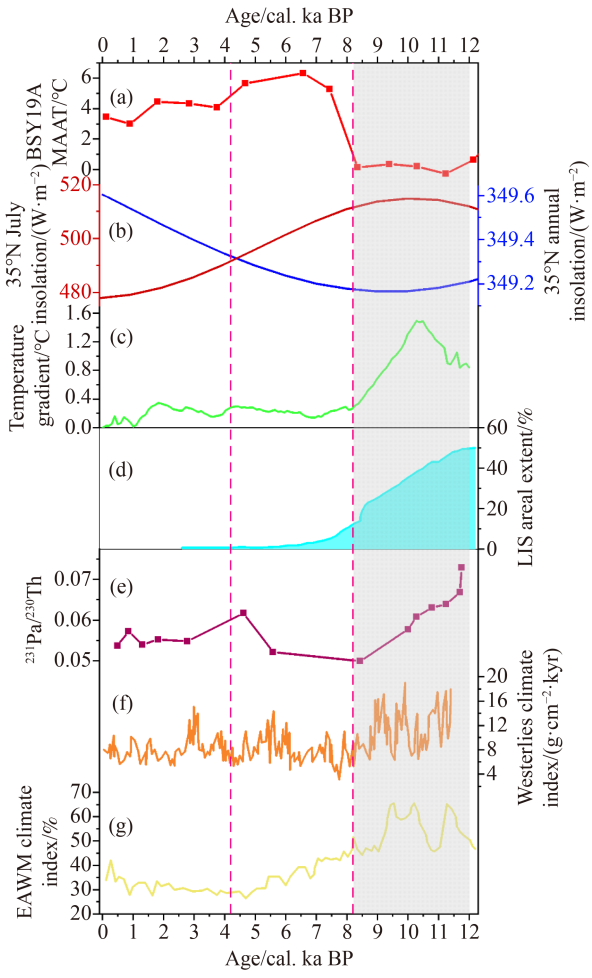

Fig. 9 Possible forcing mechanisms for Holocene temperature evolution reconstructed from the BSY19A section. (a) MBT'_{5ME}-based MAAT record from the BSY19A section (this study), (b) The ratio of $^{231}Pa/^{230}Th$ record of a sediment core from the subtropical North Atlantic Ocean (McManus et al., 2004), (c) areal extent of the LIS relative to the last glacial maximum (Dyke, 2004), (d) longitudinal temperature gradient between 30°N and 90°N (Lu et al., 2022), (e) westerlies climate index of Qinghai Lake (An et al., 2012), (f) EAWM climate index of the Huangyanghe section (Li and Morrill, 2015), (g) annual (blue line) and July (red line) solar insolation at 35°N (Laskar et al., 2004). The vertical pink lines indicate the boundaries of the early to middle, and middle to late Holocene periods (4.2 ka, 8.2 ka, respectively). The gray area represents the relatively low temperature during the early Holocene in the Ganjia Basin.

Xingyun Lake (Hou et al., 2016; Zhang et al., 2017; Wu et al., 2018; Zhang et al., 2022b). This decline coincides with a decrease in local summer insolation (Laskar et al., 2004; Fig. 9(g)). The records of magnetic susceptibility and grain size show that the influence of the EASM in the Ganga Basin increased significantly during the mid-Holocene, and gradually weakened from 3 ka (Wu et al., 2021). Sensible heat transport of warm vapor carried by the EASM is one of the important sources of heat over the TP (An et al., 2015), and which contributed to the warm climate during the mid-Holocene.

6 Conclusions

We present a reconstruction of the Holocene MAAT record based on brGDGTs indices in the Gnajia Basin in the NETP. The results show three main stages of temperature evolution, namely, low temperatures during the early Holocene (12−8 ka), a thermal maximum during the mid-Holocene (8−4 ka), and a general cooling during the late Holocene (4−0 ka). We found that this reconstructed temperature pattern is consistent with multiple records in the Northern Hemisphere. By comparing the climate forcings and feedbacks, we conclude that the lower annual solar radiation and the cooling effect of residual continental ice sheets in the Northern Hemisphere result in the low MAAT during the early Holocene. However, during the mid to late Holocene, the MAAT variability was controlled by local summer solar radiation in the Ganjia Basin.

Acknowledgments This research was supported by the National Natural Science Foundation of China (Grant Nos. 42171150 and 42130502) and the Second Tibetan Plateau Scientific Expedition and Research Program (STEP) (No. 2019QZKK0601). We sincerely thank Dr. Yanwu Duan for his constructive suggestions.

Competing interests The authors declare that they have no competing interests.

References

Alder J R, Hostetler S W (2015). Global climate simulations at 3000-year intervals for the last 21000 years with the GENMOM coupled atmosphere–ocean model. Clim Past, 11(3): 449–471

An Z S, Wu G X, Li J P, Sun Y B, Liu Y M, Zhou W J, Cai Y J, Duan A, Li L, Mao J Y, Cheng H, Shi Z G, Tan L C, Yan H, Ao H, Chang H, Feng J (2015). Global monsoon dynamics and climate change. Annu Rev Earth Planet Sci, 43(1): 29–77

An Z, Colman S M, Zhou W, Li X, Brown E T, Jull A J T, Cai Y, Huang Y, Lu X, Chang H, Song Y, Sun Y, Xu H, Liu W, Jin Z, Liu X, Cheng P, Liu Y, Ai L, Li X, Liu X, Yan L, Shi Z, Wang X, Wu F, Qiang X, Dong J, Lu F, Xu X (2012). Interplay between the Westerlies and Asian monsoon recorded in Lake Qinghai sediments since 32 ka. Sci Rep, 2(1): 619

Baker J L, Lachniet M S, Chervyatsova O, Asmerom Y, Polyak V J (2017). Holocene warming in western continental Eurasia driven by glacial retreat and greenhouse forcing. Nat Geosci, 10(6): 430–435

Beghin P, Charbit S, Dumas C, Kageyama M, Ritz C (2015). How might the North American ice sheet influence the northwestern Eurasian climate. Clim Past, 11(10): 1467–1490

Bolch T, Kulkarni A, Kääb A, Huggel C, Paul F, Cogley J G, Frey H, Kargel J S, Fujita K, Scheel M, Bajracharya S, Stoffel M (2012). The state and fate of Himalayan glaciers. Science, 336(6079): 310–314

Bova S, Rosenthal Y, Liu Z, Godad S P, Yan M (2021). Seasonal origin of the thermal maxima at the Holocene and the last interglacial. Nature, 589(7843): 548–553

Cao M, Rueda G, Rivas-Ruiz P, Trapote M C, Henriksen M, Vegas-Vilarrubia T, Rosell-Melé A (2018). Branched GDGT variability in sediments and soils from catchments with marked temperature seasonality. Org Geochem, 122: 98–114

Carlson A E, LeGrande A N, Oppo D W, Came R E, Schmidt G A, Anslow F S, Licciardi J M, Obbink E A (2008). Rapid early Holocene deglaciation of the Laurentide ice sheet. Nat Geosci, 1(9): 620–624

Cartapanis O, Jonkers L, Moffa-Sanchez P, Jaccard S L, de Vernal A (2022). Complex spatio-temporal structure of the Holocene Thermal Maximum. Nat Commun, 13(1): 5662

Chen C H, Bai Y, Fang X M, Guo H C, Meng Q Q, Zhang W L, Zhou P C, Murodov A (2019). A Late Miocene terrestrial temperature history for the northeastern Tibetan Plateau's period of tectonic expansion. Geophys Res Lett, 46(14): 8375–8386

Chen F H, Yu Z C, Yang M L, Ito E, Wang S M, Madsen D B, Huang X Z, Zhao Y, Sato T, Birks H J B, Boomer I, Chen J H, An C B, Wünnemann B (2008). Holocene moisture evolution in arid central Asia and its out-of-phase relationship with Asian monsoon history. Quat Sci Rev, 27(3): 351–364

Chen F H, Zhang J F, Liu J B, Cao X Y, Hou J Z, Zhu L P, Xu X K, Liu X J, Wang M D, Wu D, Huang L X, Zeng T, Zhang S, Huang W, Zhang X, Yang K (2020). Climate change, vegetation history, and landscape responses on the Tibetan Plateau during the Holocene: a comprehensive review. Quat Sci Rev, 243: 106444

Crampton-Flood E D, Tierney J E, Peterse F, Kirkels F M S A, Sinninghe Damste J S (2020). BayMBT: a Bayesian calibration model for branched glycerol dialkyl glycerol tetraethers in soils and peats. Geochim Cosmochim Acta, 268: 142–159

Dang X, Yang H, Naafs B D A, Pancost R D, Xie S (2016). Evidence of moisture control on the methylation of branched glycerol dialkyl glycerol tetraethers in semi-arid and arid soils. Geochim Cosmochim Acta, 189: 24–36

De Jonge C, Hopmans E C, Stadnitskaia A, Rijpstra W I C, Hofland R, Tegelaar E, Sinninghe DamstéDamsté J S S (2013). Identification of novel penta- and hexamethylated branched glycerol dialkyl glycerol tetraethers in peat using HPLC–MS2, GC–MS and GC–SMB-MS. Org Geochem, 54: 78–82

De Jonge C, Hopmans E C, Zell C I, Kim J H, Schouten S, Sinninghe Damste J S (2014). Occurrence and abundance of 6-methyl branched glycerol dialkyl glycerol tetraethers in soils: implications for palaeoclimate reconstruction. Geochim Cosmochim Acta, 141: 97–112

De Jonge C, Radujković D, Sigurdsson B D, Weedon J T, Janssens I, Peterse F (2019). Lipid biomarker temperature proxy responds to abrupt shift in the bacterial community composition in geothermally heated soils. Org Geochem, 137: 103897

Deng L H, Jia G D, Jin C F, Li S J (2016). Warm season bias of branched GDGT temperature estimates causes underestimation of altitudinal lapse rate. Org Geochem, 96: 11–17

Ding S, Xu Y, Wang Y, He Y, Hou J, Chen L, He J S (2015). Distribution of branched glycerol dialkyl glycerol tetraethers in surface soils of the Qinghai-Tibetan Plateau: implications of brGDGTs-based proxies in cold and dry regions. Biogeosciences,

12(11): 3141–3151

Dong Y J, Wu N Q, Li F J, Zhang D, Zhang Y T, Shen C M, Lu H Y (2022). The Holocene temperature conundrum answered by mollusk records from East Asia. Nature Communications, 13(1): 5153

Duan Y W, Sun Q, Werne J P, Hou J Z, Yang H, Wang Q, Khormali F, Xia D S, Chu G Q, Chen F H (2022). General Holocene warming trend in arid Central Asia indicated by soil isoprenoid tetraethers. Global Planet Change, 215: 103879

Dyke A S (2004). An outline of North American Deglaciation with emphasis on central and northern Canada. Dev Quat Res, 2: 373–424

Feng X P, Zhao C, D'Andrea W J, Hou J Z, Yang X D, Xiao X Y, Shen J, Duan Y W, Chen F H (2022). Evidence for a Relatively Warm Mid-to Late Holocene on the southeastern Tibetan Plateau. Geophys Res Lett, 49(15): e2022GL098740

Feng X P, Zhao C, D'Andrea W J, Liang J, Zhou A F, Shen J (2019). Temperature fluctuations during the Common Era in subtropical southwestern China inferred from brGDGTs in a remote alpine lake. Earth Planet Sci Lett, 510: 26–36

Han L, Li Y, Liu X, Yang H (2020). Paleoclimatic reconstruction and the response of carbonate minerals during the past 8000 years over the northeast Tibetan Plateau. Quat Int, 553: 94–103

He Y, Hou J, Wang M, Li X, Liang J, Xie S, Jin Y (2020). Temperature variation on the central Tibetan Plateau revealed by glycerol dialkyl glycerol tetraethers from the sediment record of Lake Linggo Co Since the Last Deglaciation. Front Earth Sci (Lausanne), 8: 574206

Herzschuh U, Borkowski J, Schewe J, Mischke S, Tian F (2014). Moisture-advection feedback supports strong early-to-mid Holocene monsoon climate on the eastern Tibetan Plateau as inferred from a pollen-based reconstruction. Palaeogeogr Palaeoclimatol Palaeoecol, 402: 44–54

Hou J Z, Huang Y S, Zhao J T, Liu Z H, Colman S, An Z S (2016). Large Holocene summer temperature oscillations and impact on the peopling of the northeastern Tibetan Plateau. Geophys Res Lett, 43(3): 1323–1330

Hou J, Li C G, Lee S (2019). The temperature record of the Holocene: progress and controversies. Sci Bull (Beijing), 64(9): 565–566

Immerzeel W W, Lutz A F, Andrade M, Bahl A, Biemans H, Bolch T, Hyde S, Brumby S, Davies B J, Elmore A C, Emmer A, Feng M, Fernández A, Haritashya U, Kargel J S, Koppes M, Kraaijenbrink P D A, Kulkarni A V, Mayewski P A, Nepal S, Pacheco P, Painter T H, Pellicciotti F, Rajaram H, Rupper S, Sinisalo A, Shrestha A B, Viviroli D, Wada Y, Xiao C, Yao T, Baillie J E M (2020). Importance and vulnerability of the world's water towers. Nature, 577(7790): 364–369

Immerzeel W W, van Beek L P, Bierkens M F (2010). Climate change will affect the Asian water towers. Science, 328(5984): 1382–1385

IPCC (2023). Summary for Policymakers. In: Climate Change 2021: The Physical Science Basis. Contribution of Working Group I to the Sixth Assessment Report of the Intergovernmental Panel on Climate Change [Masson-Delmotte, V., P. Zhai, A. Pirani, S. L. Connors, C. Péan, S. Berger, N. Caud, Y. Chen, L. Goldfarb, M. I. Gomis, M. Huang, K. Leitzell, E. Lonnoy, J.B.R. Matthews, T. K. Maycock, T. Waterfield, O. Yelekçi, R. Yu and B. Zhou (eds.)]. Cambridge University Press, Cambridge, United Kingdom and New York, NY, USA, pp. 3−32

Jacob T, Wahr J, Pfeffer W T, Swenson S (2012). Recent contributions of glaciers and ice caps to sea level rise. Nature, 482(7386): 514–518

Kaufman D S, Broadman E (2023). Revisiting the Holocene global temperature conundrum. Nature, 614(7948): 425–435

Kaufman D, McKay N, Routson C, Erb M, Davis B, Heiri O, Jaccard S, Tierney J, Dätwyler C, Axford Y, Brussel T, Cartapanis O, Chase B, Dawson A, de Vernal A, Engels S, Jonkers L, Marsicek J, Moffa-Sánchez P, Morrill C, Orsi A, Rehfeld K, Saunders K, Sommer P S, Thomas E, Tonello M, Tóth M, Vachula R, Andreev A, Bertrand S, Biskaborn B, Bringué M, Brooks S, Caniupán M, Chevalier M, Cwynar L, Emile-Geay J, Fegyveresi J, Feurdean A, Finsinger W, Fortin M C, Foster L, Fox M, Gajewski K, Grosjean M, Hausmann S, Heinrichs M, Holmes N, Ilyashuk B, Ilyashuk E, Juggins S, Khider D, Koinig K, Langdon P, Larocque-Tobler I, Li J, Lotter A, Luoto T, Mackay A, Magyari E, Malevich S, Mark B, Massaferro J, Montade V, Nazarova L, Novenko E, Pařil P, Pearson E, Peros M, Pienitz R, Płóciennik M, Porinchu D, Potito A, Rees A, Reinemann S, Roberts S, Rolland N, Salonen S, Self A, Seppä H, Shala S, St-Jacques J M, Stenni B, Syrykh L, Tarrats P, Taylor K, van den Bos V, Velle G, Wahl E, Walker I, Wilmshurst J, Zhang E, Zhilich S (2020). A global database of Holocene paleotemperature records. Sci Data, 7(1): 115

Laepple T, Shakun J, He F, Marcott S (2022). Concerns of assuming linearity in the reconstruction of thermal maxima. Nature, 607(7920): E12–E14

Laskar J, Robutel P, Joutel F, Gastineau M, Correia A C M, Levrard B (2004). A long-term numerical solution for the insolation quantities of the Earth. Astron Astrophys, 428(1): 261–285

Li G Q, Zhang H X, Liu X J, Yang H, Wang X Y, Zhang X J, Jonell T N, Zhang Y N, Huang X, Wang Z, Wang Y X, Yu L P, Xia D S (2020). Paleoclimatic changes and modulation of East Asian summer monsoon by high-latitude forcing over the last 130,000 years as revealed by independently dated loess-paleosol sequences on the NE Tibetan Plateau. Quat Sci Rev, 237: 106283

Li Q, Sun Q, Xie M M, Ling Y, Zhu Z Y, Zhu Q Z, Zhan N, Chu G Q (2022). Temperature variations during the past 20 ka at Huguangyan Maar Lake in tropical China and dynamic link. ESS Open Archive, August 20, 2022

Li X, Wang M, Zhang Y, Lei L, Hou J (2017). Holocene climatic and environmental change on the western Tibetan Plateau revealed by glycerol dialkyl glycerol tetraethers and leaf wax deuterium-to-hydrogen ratios at Aweng Co. Quat Res, 87(3): 455–467

Li Y, Morrill C (2015). A Holocene East Asian winter monsoon record at the southern edge of the Gobi Desert and its comparison with a transient simulation. Clim Dyn, 45(5–6): 1219–1234

Liu Y, Zhang M, Liu Z, Xia Y, Huang Y, Peng Y, Zhu J (2018). A possible role of dust in resolving the Holocene temperature conundrum. Sci Rep, 8(1): 4434

Liu Z, Zhu J, Rosenthal Y, Zhang X, Otto-Bliesner B L, Timmermann A, Smith R S, Lohmann G, Zheng W, Elison Timm O (2014). The Holocene temperature conundrum. Proc Natl Acad Sci USA,

111(34): E3501–E3505

Lu W, Zhao X H, Feng X S, Xiang N B, Du Z L, Zhang W T (2022). Temporal and spatial response of Holocene temperature to solar activity. Quat Int, 613: 39–45

Marcott S A, Shakun J D, Clark P U, Mix A C (2013). A reconstruction of regional and global temperature for the past 11300 years. Science, 339(6124): 1198–1201

Marsicek J, Shuman B N, Bartlein P J, Shafer S L, Brewer S (2018). Reconciling divergent trends and millennial variations in Holocene temperatures. Nature, 554(7690): 92–96

McManus J F, Francois R, Gherardi J M, Keigwin L D, Brown-Leger S (2004). Collapse and rapid resumption of Atlantic meridional circulation linked to deglacial climate changes. Nature, 428(6985): 834–837

Meyer H, Opel T, Laepple T, Dereviagin A Y, Hoffmann K, Werner M (2015). Long-term winter warming trend in the Siberian Arctic during the mid- to late Holocene. Nat Geosci, 8(2): 122–125

Mjell T L, Ninnemann U S, Eldevik T, Kleiven H F (2015). Holocene multidecadal- to millennial-scale variations in Iceland-Scotland overflow and their relationship to climate. Paleoceanography, 30(5): 558–569

Naafs B D A, Gallego-Sala A V, Inglis G N, Pancost R D (2017). Refining the global branched glycerol dialkyl glycerol tetraether (brGDGTs) soil temperature calibration. Org Geochem, 106: 48–56

Neckel N, Kropáček J, Bolch T, Hochschild V (2014). Glacier mass changes on the Tibetan Plateau 2003–2009 derived from ICES at laser altimetry measurements. Environ Res Lett, 9(1): 014009

Ning D L, Zhang N L, Shulmeister J, Chang J, Sun W W, Ni Z Y (2019). Holocene mean annual air temperature (MAAT) reconstruction based on branched glycerol dialkyl glycerol tetraethers from Lake Ximenglongtan, southwestern China. Org Geochem, 133: 65–76

Opitz S, Zhang C, Herzschuh U, Mischke S (2015). Climate variability on the south-eastern Tibetan Plateau since the Lateglacial based on a multiproxy approach from Lake Naleng – comparing pollen and non-pollen signals. Quat Sci Rev, 115: 112–122

Osman M B, Tierney J E, Zhu J, Tardif R, Hakim G J, King J, Poulsen C J (2021). Globally resolved surface temperatures since the Last Glacial Maximum. Nature, 599(7884): 239–244

Pang H, Hou S, Zhang W, Wu S, Jenk T M, Schwikowski M, Jouzel J (2020). Temperature trends in the northwestern Tibetan Plateau constrained by ice core water isotopes over the past 7000 years. J Geophys Res Atmos, 125(19): e2020JD032560

Park H S, Kim S J, Stewart A L, Son S W, Seo K H (2019). Mid-Holocene Northern Hemisphere warming driven by Arctic amplification. Sci Adv, 5(12): eaax8203

Peterse F, Prins M A, Beets C J, Troelstra S R, Zheng H B, Gu Z Y, Schouten S, Damsté J S S (2011). Decoupled warming and monsoon precipitation in East Asia over the last deglaciation. Earth Planet Sci Lett, 301(1–2): 256–264

Peterse F, van der Meer J, Schouten S, Weijers J W H, Fierer N, Jackson R B, Kim J H, Sinninghe Damsté J S (2012). Revised calibration of the MBT-CBT paleotemperature proxy based on branched tetraether membrane lipids in surface soils. Geochim Cosmochim Acta, 96: 215–229

Qiu J (2008). China: the third pole. Nature, 454(7203): 393–396

Rao Z G, Shi F X, Li Y X, Huang C, Zhang X Z, Yang W, Liu L D, Zhang X P, Wu Y (2020). Long-term winter/summer warming trends during the Holocene revealed by α-cellulose $\delta^{18}O/\delta^{13}C$ records from an alpine peat core from central Asia. Quat Sci Rev, 232: 106217

Renssen H, Seppä H, Heiri O, Roche D M, Goosse H, Fichefet T (2009). The spatial and temporal complexity of the Holocene thermal maximum. Nat Geosci, 2(6): 411–414

Schouten S, Hopmans E C, Sinninghe Damsté J S (2013). The organic geochemistry of glycerol dialkyl glycerol tetraether lipids: a review. Org Geochem, 54: 19–61

Shang X S, Jin Y P (2012). Characteristics of natural grassland vegetation types and their distribution patterns in Xiahe, Gannan. Prataculture & Animal Husbandry, 194(01): 39–40 (in Chinese)

Sun W, Zhao S, Pei H, Yang H (2019). The coupled evolution of mid- to late Holocene temperature and moisture in the southeast Qaidam Basin. Chem Geol, 528: 119282

Sun X H, Zhao C, Zhang C, Feng X P, Yan T L, Yang X D, Shen J (2021). Seasonality in Holocene temperature reconstructions in Southwestern China. Paleoceanogr Paleoclimatol, 36(1): e2020PA004025

Sun Y B, Clemens S C, Morrill C, Lin X P, Wang X L, An Z S (2012). Influence of Atlantic meridional overturning circulation on the East Asian winter monsoon. Nat Geosci, 5(1): 46–49

Thompson A J, Zhu J, Poulsen C J, Tierney J E, Skinner C B (2022). Northern Hemisphere vegetation change drives a Holocene thermal maximum. Sci Adv, 8(15): eabj6535

Véquaud P, Thibault A, Derenne S, Anquetil C, Collin S, Contreras S, Nottingham A T, Sabatier P, Werne J P, Huguet A (2022). FROG: a global machine-learning temperature calibration for branched GDGTs in soils and peats. Geochim Cosmochim Acta, 318: 468–494

Wang H S, Gao P, Yang R, Nie J S, Cao B, Zhou A F, Pan B T, Chen L, Peng T J (2022). Correlation between brGDGTs distribution and elevation from the eastern Qilian Shan. Front Earth Sci (Lausanne), 10: 844026

Wang H Y, Liu W G (2021). Soil temperature and brGDGTs along an elevation gradient on the northeastern Tibetan Plateau: a test of soil brGDGTs as a proxy for paleoelevation. Chem Geol, 566: 120079

Wang H, An Z, Lu H, Zhao Z, Liu W (2020). Calibrating bacterial tetraether distributions towards in situ soil temperature and application to a loess-paleosol sequence. Quat Sci Rev, 231: 106172

Wang M D, Hou J Z, Duan Y W, Chen J H, Li X M, He Y, Lee S Y, Chen F H (2021). Internal feedbacks forced Middle Holocene cooling on the Qinghai-Tibetan Plateau. Boreas, 50(4): 1116–1130

Wang M Y, Zheng Z, Man M L, Hu J F, Gao Q Z (2017). Branched GDGT-based paleotemperature reconstruction of the last 30,000 years in humid monsoon region of southeast China. Chem Geol, 463: 94–102

Weijers J W H, Schouten S, van den Donker J C, Hopmans E C, Sinninghe Damste J S (2007). Environmental controls on bacterial tetraether membrane lipid distribution in soils. Geochim Cosmochim Acta, 71(3): 703–713

Wu D, Chen X M, Lv F Y, Brenner M, Curtis J, Zhou A F, Chen J H,

Abbott M, Yu J Q, Chen F H (2018). Decoupled early Holocene summer temperature and monsoon precipitation in southwest China. Quat Sci Rev, 193: 54–67

Wu D, Zhang C B, Wang T, Liu L, Zhang X J, Yuan J Z, Yang S L, Chen F H (2021). East-west asymmetry in the distribution of rainfall in the Chinese Loess Plateau during the Holocene. Catena, 207: 105626

Yan T L, Zhao C, Yan H, Shi G, Sun X S, Zhang C, Feng X P, Leng C C (2021). Elevational differences in Holocene thermal maximum revealed by quantitative temperature reconstructions at ~30°N on eastern Tibetan Plateau. Palaeogeogr Palaeoclimatol Palaeoecol, 570: 110364

Yang H, Pancost R D, Dang X, Zhou X, Evershed R P, Xiao G Q, Tang C Y, Gao L, Guo Z T, Xie S C (2014). Correlations between microbial tetraether lipids and environmental variables in Chinese soils: optimizing the paleo-reconstructions in semi-arid and arid regions. Geochim Cosmochim Acta, 126: 49–69

Yao T D, Wu G J, Xu B Q, Wang W C, Gao J, An B S (2019). Asian water tower change and its impacts. Bull Chinese Academy Sci, 34(11): 1201–1209 (in Chinese)

Zhang C B, Wu D, Chen X M, Yuan Z J, Chen F H (2022a). A preliminary study of the strata and age of ancient agricultural terraces in the Ganjia Basin, northeastern Tibetan Plateau. Acta Geogr Sin, 77(1): 66–78 (in Chinese)

Zhang C, Zhao C, Yu S Y, Yang X D, Cheng J, Zhang X J, Xue B, Shen J, Chen F H (2022b). Seasonal imprint of Holocene temperature reconstruction on the Tibetan Plateau. Earth Sci Rev, 226: 103927

Zhang E L, Chang J, Cao Y M, Sun W W, Shulmeister J, Tang H Q, Langdon P G, Yang X D, Shen J (2017). Holocene high-resolution quantitative summer temperature reconstruction based on subfossil chironomids from the southeast margin of the Qinghai-Tibetan Plateau. Quat Sci Rev, 165: 1–12

Zhang W C, Wu H B, Cheng J, Geng J Y, Li Q, Sun Y, Yu Y Y, Lu H Y, Guo Z T (2022c). Holocene seasonal temperature evolution and spatial variability over the Northern Hemisphere landmass. Nat Commun, 13(1): 5334

Zhang X, Chen F (2021). Non-trivial role of internal climate feedback on interglacial temperature evolution. Nature, 600(7887): E1–E3

Zhao B Y, Hu J F, Liu F H, Chen W, Chen W M (2021a). Variation of temperature in Lake Nanyi sediments from the lower Yangtze River region since the last 12.0 ka B. P. Quat Sci, 41(4): 1044–1055 (in Chinese)

Zhao C, Rohling E J, Liu Z, Yang X, Zhang E, Cheng J, Liu Z, An Z, Yang X, Feng X, Sun X, Zhang C, Yan T, Long H, Yan H, Yu Z, Liu W, Yu S Y, Shen J (2021b). Possible obliquity-forced warmth in southern Asia during the last glacial stage. Sci Bull (Beijing), 66(11): 1136–1145

Zhao H, Huang C C, Wang H Y, Liu W G, Qiang X K, Xu X W, Zheng Z K, Hu Y, Zhou Q, Zhang Y Z, Guo Y Q (2018). Mid-late Holocene temperature and precipitation variations in the Guanting Basin, upper reaches of the Yellow River. Quat Int, 490: 74–81

Zhao J J, Tsai V C, Huang Y S (2022). A nonlinear model for resolving the temperature bias of branched glycerol dialkyl glycerol tetraether (brGDGTs) temperature proxies. Geochim Cosmochim Acta, 327: 158–169